ACS OMEGA

http://pubs.acs.org/journal/acsodf

Article

Microwave- and Formaldehyde-Assisted Synthesis of Ag−Ag_3PO_4 with Enhanced Photocatalytic Activity for the Degradation of Rhodamine B Dye and Crude Oil Fractions

Emmanuel Nyankson,* Reuben Amedalor, Gauthaman Chandrabose, Michael Coto, Satheesh Krishnamurthy, and R. Vasant Kumar

Cite This: *ACS Omega* 2020, 5, 13641−13655

Read Online

ACCESS | Metrics & More | Article Recommendations

ABSTRACT: The release of crude oil and water-soluble dyes into our marine environment is a major global problem. An efficient semiconductor Ag−Ag_3PO_4 photocatalyst was synthesized using formaldehyde as a reducing agent to form surface active Ag on Ag_3PO_4 under microwave radiation for heating, and its potential in destroying environmental pollutants has been examined. The diffuse reflectance spectroscopy of Ag−Ag_3PO_4 revealed an enhanced absorption in the visible light region. The rate of photocatalytic degradation of rhodamine B by Ag−Ag_3PO_4 was over 4-fold compared to Ag_3PO_4. The potential application of Ag−Ag_3PO_4 in oil spill remediation was also examined through photocatalytic degradation of benzene, *n*-hexane, and 1:1 v/v benzene/methanol crude oil-soluble fractions. UV−vis and gas chromatography−mass spectrometry analysis of the crude oil components after visible light irradiation showed excellent degradation. The photocatalytic efficiency enhancement of Ag−Ag_3PO_4 is attributed to the excellent electron trapping of silver nanoparticles deposited on the surface of Ag_3PO_4. This work will motivate future studies to develop recyclable visible light photocatalysts for many applications.

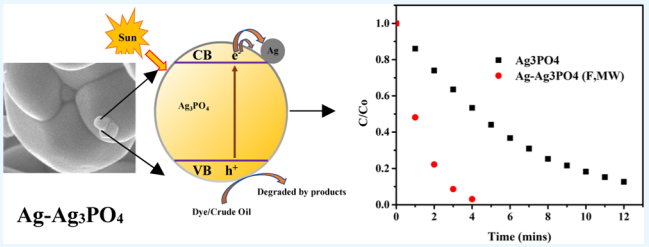

1. INTRODUCTION

Environmental pollution and its effects on human civilization are a major threat globally. For example, oil spillages and the discharge of dyes into water bodies used in painting, printing, plastic, textile, pharmaceutical, food processing, and so forth have a devastating effect on the environment and affect the survival of humans and aquatic species. For oil spillages, remediation technologies such as in situ burning, the application of chemical dispersants, and mechanical containment and collection are employed to reduce their environmental impact.[1] Although chemical dispersants are widely accepted as a response strategy for large-scale oil spills, they are reportedly ineffective in remediating the water-soluble components of crude oil.[1h,2] Therefore, there is a strong need for a remediation strategy that is effective at treating the water-soluble components of crude oil (aromatics). Additionally, environmental pollution by water-soluble dyes can be tackled through promoting adsorption,[3] followed by photocatalytic treatments.[4]

Interest in photocatalytic processes presents an attractive solution to numerous wastewater and oil spill remediation challenges. Photocatalysis has been reported to be an effective strategy using materials that are stable and environmentally friendly for environmental pollution control.[5] Photocatalysis involves the following steps: (a) a photocatalyst is irradiated using photons with energy greater than or equal to the band gap energy of the photocatalyst, (b) electron−hole pair is generated as a result of the photoexcitation of electrons from the valence band (VB) to the conduction band (CB), (c) the generated holes and electrons are transported to the surface of the photocatalyst where they are utilized in the creation of reactive oxygen species. The high oxygen potential observed in photocatalytic processes allows for complete breakdown of organic contaminants. In addition, the use of sunlight makes it attractive solution environmentally. The most widely used semiconductor photocatalyst material is based on TiO_2.[6] TiO_2 is relatively cheap, very stable, and readily available and has high activation.[7] The band gap of TiO_2 is ca. 3.2 eV. This large value has restricted its application to the UV region of the electromagnetic spectrum. Because ultraviolet light represents approximately 4−5% of solar radiation that arrives on the earth's surface, many researchers have focused on developing

Received: February 14, 2020
Accepted: April 3, 2020
Published: June 1, 2020

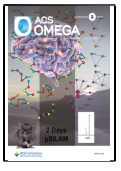

https://dx.doi.org/10.1021/acsomega.0c00670
ACS Omega 2020, 5, 13641−13655

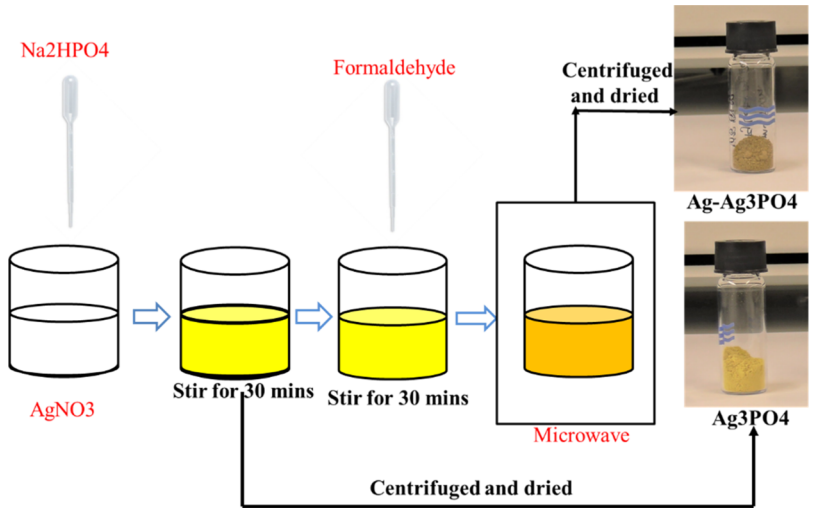

Figure 1. Schematic presentation of Ag_3PO_4 modified with Ag using formaldehyde and MW.

visible light active photocatalysts.[8] However, TiO_2 and many photocatalysts have limitations because of wide band gap, poor quantum efficiency under visible light, and faster decay of photoexcited electron−hole pairs. These challenges can be addressed by developing a new visible light active photocatalyst or by coupling different photocatalysts to create heterostructures.[9] Ag_3PO_4 which is a visible light active semiconductor in the environmental remediation of water-soluble dyes has been investigated, and direct and indirect band gaps of Ag_3PO_4 are reported to be 2.34 and 2.36 eV, respectively.[10] Ag_3PO_4 has a CB and a deep VB located at +0.45 V versus NHE (normal hydrogen electrode) and +2.9 V versus NHE, respectively,[11] implying that reduction of Ag_3PO_4 to Ag^0 is thermodynamically more favorable than the reduction of H^+ to H_2 under light irradiation in water.[7] Hence, the stability of Ag_3PO_4 is an issue. The limited photostability of Ag_3PO_4 has negatively affected its practical application in photocatalysis.

Hence, many researchers are studying Ag_3PO_4 with the main objective of reducing photocorrosion and enhancing the photocatalytic efficiency for practical applications. In order to enhance the photostability and efficiency of Ag_3PO_4, coupling of Ag_3PO_4 with either a metal or a semiconductor is proposed. Ag_3PO_4 modified through the introduction of a heterojunction can significantly outperform Ag_3PO_4 single phases. Electron−hole recombination is reduced when the electron and hole migrate from a semiconductor to the semiconductor.[8a,12] The reduction of the electron−hole recombination will increase the life span of the photogenerated electrons and holes. In addition, the localized surface plasmon resonance of the silver nanoparticles on Ag_3PO_4 can enhance the photocatalytic efficiency and stability.[13] Coupling Ag_3PO_4 with Ag_2S resulted in an enhanced photocatalytic degradation of methyl orange when compared to pure Ag_3PO_4.[14] $Ag_3PO_4/Co_3(PO4)_2$@Ag and Ag_3PO_4/Ag_2MoO_4 photocatalysts with enhanced degradation of organic pollutants have been reported.[15] Hou et al. synthesized different Ag_3PO_4 interfaces including combinations of Ag_3PO_4−Ag and Ag_3PO_4−AgBr. The composite's photocatalytic activity rate showed a 200% enhancement, compared to that of Ag_3PO_4.[16] Liu et al. developed a one-pot pyridine-assisted hydrothermal synthesis method for Ag/Ag_3PO_4.[7] Another synthesis route for Ag/Ag_3PO_4 involving exchange of ions between Na_2HPO_4 and $AgNO_3$ followed by a photoreduction route has been reported.[17] Ag/Ag_3PO_4/rGO microspheres with enhanced removal efficiency of Cr(IV) have also been recently reported.[18] In all these, the photocatalytic efficiency and photostability of Ag_3PO_4 were improved by combining it with Ag.

In this work, we show for the first time that a new silver phosphate nanocomposite is synthesized using formaldehyde, and the nanocomposite efficiently degrades crude oil fractions. We have synthesized Ag−Ag_3PO_4 with enhanced photocatalytic efficiency and photostability using formaldehyde and microwave (MW) radiation. Rhodamine B dye and crude oil fractions (benzene, *n*-hexane, and 1:1 v/v methanol/benzene-soluble fractions) were chosen as the model pollutants to examine the photocatalytic efficiency of Ag−Ag_3PO_4 in aqueous media under visible light irradiation. The results from this study showed that the Ag−Ag_3PO_4 photocatalyst degrades rhodamine B dye and crude oil fractions with high photocatalytic efficiency. It is worth noting that the model pollutants themselves are encountered as real pollutants because of human activities, and thus, the data obtained are significant for direct applications.

2. RESULTS AND DISCUSSION

An ion-exchange method was used to synthesize Ag_3PO_4 and decorated with Ag by chemical reduction of the excess $AgNO_3$ used in the synthesis of Ag_3PO_4 with an organic compound (formaldehyde). Ag_3PO_4 suspended in the excess $AgNO_3$ solution with formaldehyde was then microwaved. The solution was then centrifuged, and the precipitate was collected and dried at 70 °C. Ag_3PO_4 turned dark yellow/brownish after microwaving (Figure 1). This change in color with respect to pure Ag_3PO_4 suggests that the synthesized Ag_3PO_4 is decorated with Ag, and the resulting composite materials have acquired the ability to absorb light. This process is schematically represented in Figure 1.

The diffuse reflectance spectroscopy (DRS) analysis of the synthesized Ag_3PO_4 decorated with Ag using different volumetric amounts of formaldehyde and MW time of 3 min is presented in Figure 2. The DRS of the Ag_3PO_4 composite material revealed an enhanced absorption from 20 to 63% in the visible light region. The absorption increases with the increasing volume of formaldehyde used in the synthesis but leveled off after the addition of 8 mL of formaldehyde. The spectra showed that the addition of formaldehyde did not have

https://dx.doi.org/10.1021/acsomega.0c00670
ACS Omega 2020, 5, 13641−13655

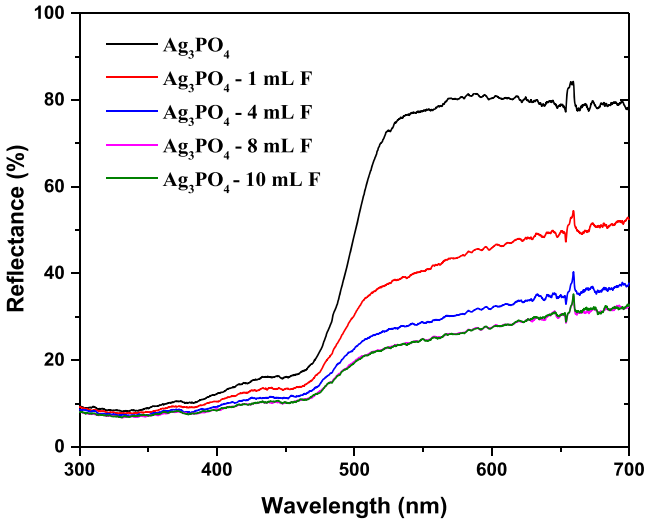

Figure 2. DRS of Ag_3PO_4 and Ag_3PO_4 modified with Ag at different volumes of formaldehyde used for the modification.

a dramatic effect on the optical band gap of Ag_3PO_4. The optical band gap of Ag_3PO_4 and Ag_3PO_4 modified using 4 mL of formaldehyde [Ag−Ag_3PO_4(F,MW)] was estimated with the Kubelka−Munk method, and the plot is represented in Figure 3. In [Ag−Ag_3PO_4(F,MW)], F and MW represent formaldehyde and MW, respectively. From Figure 3, 2.47 and 2.41 eV were the estimated optical band gaps for Ag_3PO_4 and Ag−Ag_3PO_4, respectively.

Dye degradation experiments were conducted using rhodamine B dye. A 300 W tungsten halogen lamp was used to illuminate the catalyst. The degradation efficiency as well as the pseudo-first-order rate constants is presented in Figure 4. The rate constants were estimated from eq 1 according to the Langmuir−Hinshelwood kinetics[19]

$$\ln \frac{[C]}{[C_o]} = -kt \quad (1)$$

where C and C_o are the concentrations of the dye at time t min and 0 min, respectively, and k (min^{-1}) is the pseudo-first-order rate constant. The percent degradation as well as the rate constant increased significantly upon modification with Ag (Figure 4).

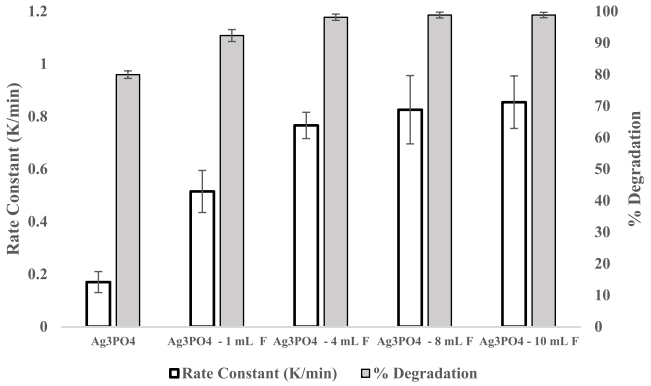

Figure 4. Effect of formaldehyde on the rate constant and degradation efficiency of rhodamine B.

The first two bars show the rate constant and the degradation efficiency of bare Ag_3PO_4, giving a % degradation and rate constant of 79.9% and 0.1696 min^{-1}, respectively, in 10 min. The results show a dramatic enhancement in the photocatalytic activity upon the addition of formaldehyde, followed by microwaving for 3 min. Upon the addition of 1 mL of formaldehyde, the % degradation and rate constant increased to 92.3% and 0.5143 min^{-1}, respectively. Further increase in the volumetric amount of formaldehyde to 10 mL resulted in a % degradation and rate constant of 98.8% and 0.854 min^{-1}, respectively. There was no significant difference in the photocatalytic activity of the composite material synthesized with 8 and 10 mL of formaldehyde when the values reached a plateau. The photocatalytic activity (rate constant) of Ag_3PO_4 therefore increased over 400% upon modification with surface Ag.

The above experiments were conducted using 3 min of microwaving time. The effect of microwaving time on optical properties and photocatalytic activity was examined. By increasing the microwaving time from 3 to 5 min, the absorption of light increased slightly in the visible region (Figure 5). The nature of the DRS shows that the band gap remained unchanged upon increasing the microwaving time. A scanning electron microscopy (SEM image) (Figure 8—presented later in this article) revealed an extreme etching of Ag−Ag_3PO_4. Increasing the microwaving time therefore affected the surface morphology.

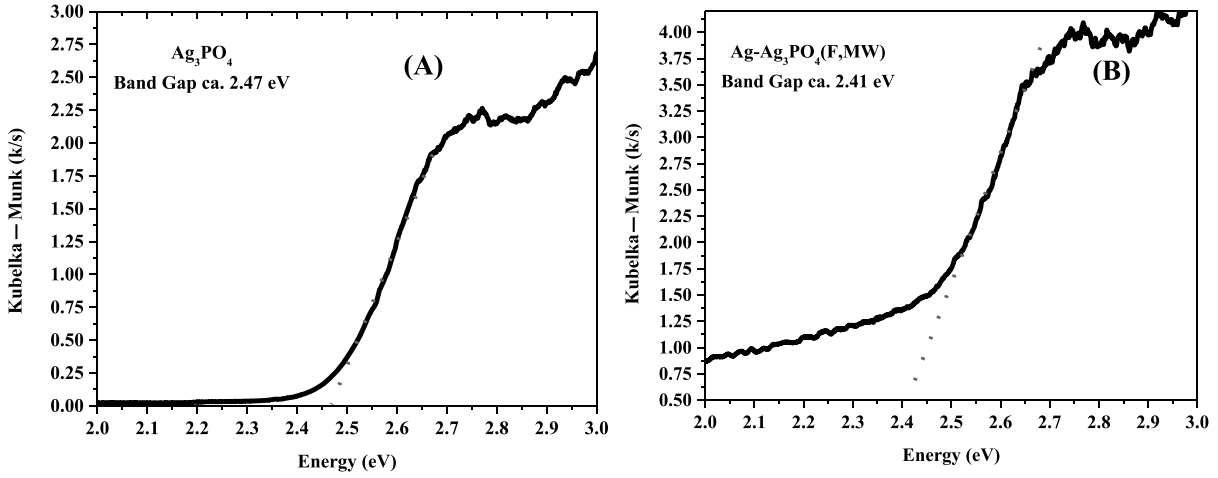

Figure 3. Generated plots from the Kubelka−Munk theory for (A) Ag_3PO_4 and (B) Ag−Ag_3PO_4(F,MW).

https://dx.doi.org/10.1021/acsomega.0c00670
ACS Omega 2020, 5, 13641−13655

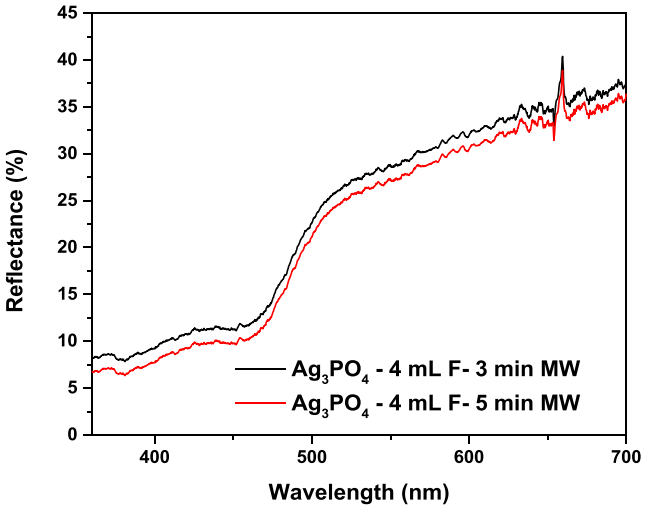

Figure 5. Effect of microwaving time on optical properties.

From Figure 6, an increase in the microwaving time resulted in a slight decrease in the degradation efficiency from 98 to

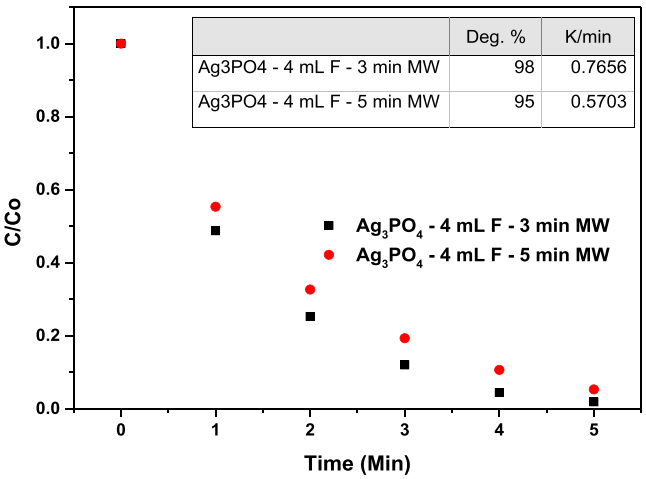

	Deg. %	K/min
Ag3PO4 - 4 mL F - 3 min MW	98	0.7656
Ag3PO4 - 4 mL F - 5 min MW	95	0.5703

Figure 6. Effect of microwaving time on photocatalytic activity.

95%. The rate constant also decreased from 0.7656 to 0.5703 min^{-1}. A similar trend was observed for all the samples synthesized with different volumetric amounts of formaldehyde.

X-ray photoelectron spectroscopy (XPS) analysis was conducted to confirm that the sample prepared using formaldehyde and MW (Ag_3PO_4−10 mL F−3 min MW) resulted in the formation of metallic Ag nanoparticles deposited on Ag_3PO_4. The survey scan of the sample shows the characteristic peaks of P 2p (132.5 eV), Mo 3d (225.0 and 227.9 eV), C 1s (284.8 eV), Ag 3d (367.5 and 373.5 eV), O 1s (531.1 eV), Ag 3p (574.1 eV), and O KLL (743 eV) (Figure 7A). The Mo 3d peak is contributed by the sample holder. The deconvoluted spectra for Ag $3d_{5/2}$ and Ag $3d_{3/2}$ (Figure 7B) show four major peaks at 367.26 eV (Ag^+ $3d_{5/2}$), 373.26 eV (Ag^+ $3d_{3/2}$), 367.87 eV (Ag^0 $3d_{5/2}$), and 373.87 eV (Ag^0 $3d_{3/2}$), in which Ag^+ and Ag^0 correspond to Ag_3PO_4 and metallic Ag, respectively.[16,20] In the spectra, both Ag^+ and Ag^0 show spin−orbit splitting with an energy separation (Δ_E) of 6.0 eV. The result shows the formation of reduced metallic Ag, and from the peak area percentage value, it is approximated that the ratio of Ag^0 to Ag^+ is 1:2. In Figure 7C, the peak at 532.54 eV is attributed to adsorbed oxygen, while the major peak at 530.72 eV is due to lattice oxygen.[20] The K alpha prime (Kα') peak at 364.52 eV (Figure 7B) and 527.74 eV (Figure 7C) is due to a nonmonochromatic X-ray source.[21] The binding energy peak position at 132.52 eV can be ascribed to P 2p, corresponding to P^{5+} in Ag_3PO_4 (Figure 7D).[22] The XPS results confirmed the creation of silver nanoparticles on the surface of Ag_3PO_4. The samples prepared with formaldehyde and MW radiation were therefore designated as Ag−Ag_3PO_4.

The SEM images of Ag_3PO_4 and Ag−Ag_3PO_4 photocatalysts are presented in Figure 8. The Ag_3PO_4 particles exhibited an irregular spherical morphology with a nonuniform diameter. The particle sizes were estimated to be between 200 and 500 nm. The composite Ag−Ag_3PO_4 exhibited a similar morphology but with the deposits of Ag nanoparticles attached to the surface of Ag_3PO_4 (Figure 8B). The energy-dispersive X-ray spectroscopy (EDX) of Ag_3PO_4 and Ag−Ag_3PO_4 is presented in Figure 8C−F. The EDX mapping of Ag_3PO_4 (Figure 8C,D) revealed even distribution of the elements present in Ag_3PO_4. The silver composition was estimated to be 74 wt %, and it is close to the theoretical value of ca. 77 wt %. For Ag_3PO_4 modified using formaldehyde and MW irradiation (Figure 8E,F), the EDX mapping revealed a higher concentration of Ag (blue color) with an estimated Ag wt % of 83. This confirms the formation of Ag on the surface of Ag_3PO_4 as deduced from the XPS analysis. EDX analysis of the smaller nanoparticle deposits on the surface of Ag_3PO_4 revealed that it has higher concentrations of Ag and a relatively lower concentration of phosphorus and oxygen.

The SEM images of the composite Ag−Ag_3PO_4 synthesized by increasing the MW irradiation time from 3 to 5 min revealed extreme etching (patches) of the Ag_3PO_4 surface. SEM−EDX analysis of the patches that appeared on the surface of Ag_3PO_4 revealed a higher concentration of silver (Figure 9) and lower concentrations of phosphorus and oxygen. The concentration of silver for two different regions in Figure 9A,B was estimated to be 95.2 and 84.9 wt %, respectively. This depicts inhomogeneous silver distribution on the surface of Ag_3PO_4.

The X-ray diffraction (XRD) pattern (Figure 10) for Ag_3PO_4 has a well-defined crystalline Ag_3PO_4 and exhibits a body-centered cubic crystal structure of Ag_3PO_4 (JCPDS no. 06-0505). Despite the increase in the silver concentration on the surface of Ag_3PO_4, XRD spectra for Ag_3PO_4 and that of Ag−Ag_3PO_4(F,MW) were similar without the appearance of Ag peaks. Because the crystal structure of Ag_3PO_4 was preserved for Ag−Ag_3PO_4 despite the relatively lower concentrations of phosphorus and oxygen detected by the EDX analysis, it can be concluded that the modification of Ag_3PO_4 in the presence of formaldehyde and MW radiation was restricted to the surface of Ag_3PO_4. Coto et al. reported a similar observation when they decorated the surface of a 25 nm TiO_2 nanoparticle with Ag nanoparticles using formaldehyde.[19] Reduction of Ag^+ into Ag^0 using formaldehyde and conventional heating resulted in the formation of a thin layer of Ag nanoparticle coating on the surface of TiO_2. Unlike XPS, XRD could not detect the presence of Ag nanoparticles. This further confirms that the reduction of Ag^+ to Ag happened only on the surface of the Ag_3PO_4 particles. That is, the synthesis method adopted resulted in the surface of Ag_3PO_4 particles being coated with a thin layer of Ag nanoparticles. Because XPS is a surface-sensitive characterization technique (~10 nm), the

https://dx.doi.org/10.1021/acsomega.0c00670
ACS Omega 2020, 5, 13641−13655

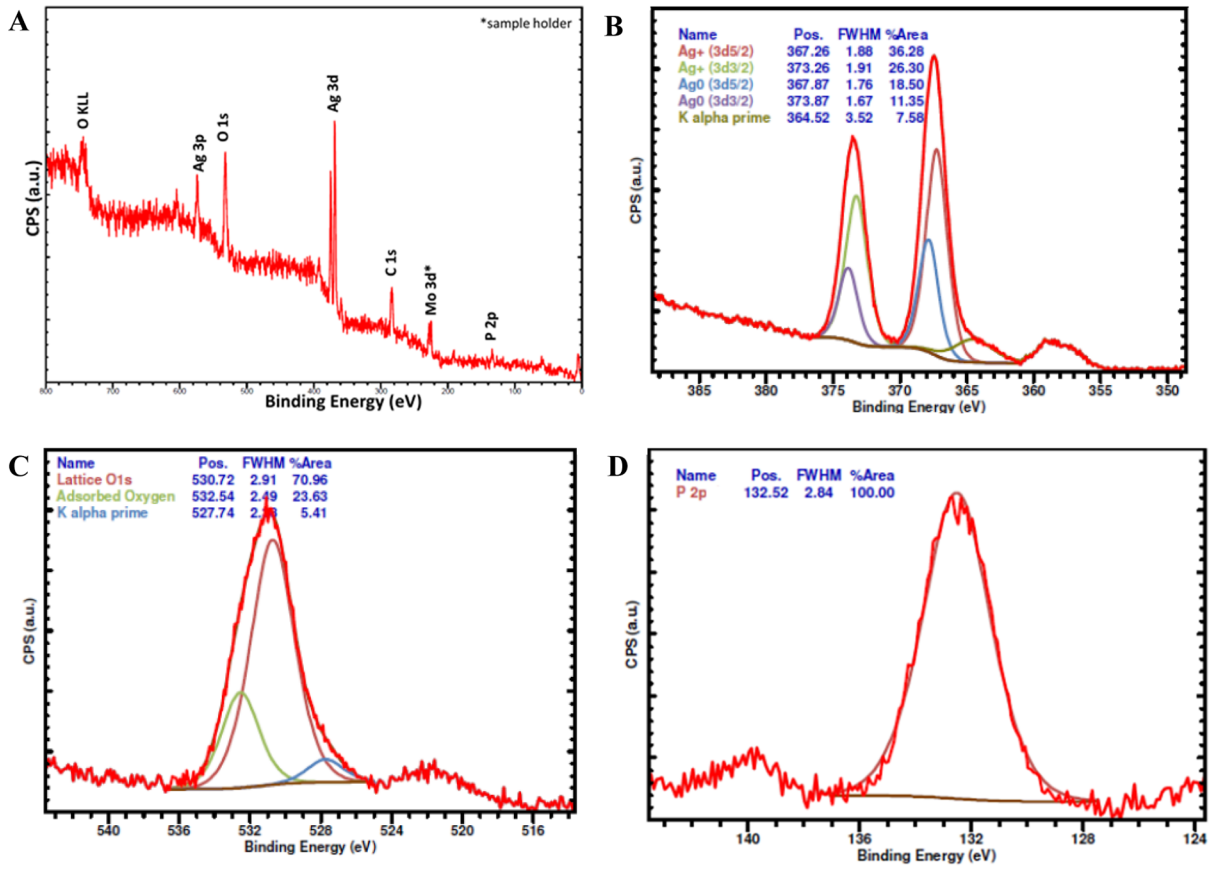

Figure 7. XPS analysis of Ag−Ag_3PO_4 (F, MW = 3 min). (A) Spectrum showing all the components of Ag−Ag_3PO_4 (F, MW = 3 min), (B) Ag+ $3d_{5/2}$ and $3d_{3/2}$ peaks confirming the presence of Ag^0, (C) XPS spectrum for O 1s, and (D) XPS spectrum for P 2p.

presence of metallic Ag nanoparticles could be detected. However, XRD is a bulk-sensitive characterization technique, and the presence of metallic Ag nanoparticles in very low concentrations (<∼5%) when compared to the bulk Ag_3PO_4 could not be detected. The thin Ag nanoparticle coating and the rough surface morphology produced from the MW radiation are responsible for the relatively higher photocatalytic activity of Ag−Ag_3PO_4 when compared with that of Ag−Ag_3PO_4 synthesized using other methods. Surface etching of Ag−Ag_3PO_4 by the MW radiation resulted in surface morphology that aids in the higher separation and transfer efficiency of the photogenerated holes and electrons.[23]

Different parameters were investigated for their effect on the photocatalytic activity of the modified and bare Ag_3PO_4. Can the deposition of Ag on the surface of Ag_3PO_4 occur by heating the precipitated Ag_3PO_4 in formaldehyde and excess $AgNO_3$ solution instead of microwaving? The results show that the photocatalytic efficiency of Ag_3PO_4 can be enhanced by conventional heating (heating in a water bath at 80 °C) of Ag_3PO_4 in formaldehyde and excess $AgNO_3$. However, the samples prepared by heating [Ag−Ag_3PO_4(F,Heating)] had a relatively lower photocatalytic activity (Figure 11) and rate constant (Figure 12) when compared to [Ag−Ag_3PO_4(F,MW)]. It has been reported that MW radiation can create Ag nanoparticles from $AgNO_3$ solution even in the absence of a reducing agent.[24] The calculated rate constant (0.5581 min^{-1}) was however higher than that of the unmodified Ag_3PO_4 (0.1696 min^{-1}). It is therefore probable that the MW radiation aided in the generation of more Ag nanoparticles. This observation implies that a heat source (either through microwaving or conventional heating) is needed in the modification process. The extreme etching (patches) observed in the [Ag−Ag_3PO_4(F,MW)] samples (Figure 9) was not observed in [Ag−Ag_3PO_4(F,Heating)], which indicates that the etching resulted from the MW radiation. The MW heating increases the rate of heating versus the water bath, thereby promoting rapid reduction of silver salts and nucleation over growth. This reduced the particle size of Ag while increasing the etching. As already mentioned, the etching of Ag_3PO_4 resulted in a surface morphology that has been reported to promote the transfer efficiency and separation of photogenerated holes and electrons.[23] The EDX analysis of the few patches (Figure 13A,C) observed with the heated samples has a relatively lower silver concentration (ca. 67.4 wt %) when compared with that of [Ag−Ag_3PO_4(F,MW)]. It should however be noted that the smooth surface of [Ag−Ag_3PO_4(F,Heating)] has a relatively higher Ag concentration (80.8 wt %) (Figure 13B,C). The photocatalyst obtained without microwaving or heating but with the addition of formaldehyde [Ag−Ag_3PO_4(F)] showed a photocatalytic activity (k = 0.432 min^{-1}) that was higher than that of bare Ag_3PO_4 but lower than that of [Ag−Ag_3PO_4(F,Heating)] and [Ag−Ag_3PO_4(F,MW)]. This implies that MW radiation and conventional heating influenced the photocatalytic activity of the modified Ag_3PO_4.

After precipitating Ag_3PO_4, formaldehyde was added, and the entire mixture was stirred for 30 min. The liquid phase was decanted, and the precipitated photocatalyst was dispersed in DI water and microwaved. This photocatalyst was designated as [Ag−Ag_3PO_4(F-Decanting,MW)]. As can be seen in Figures

https://dx.doi.org/10.1021/acsomega.0c00670
ACS Omega 2020, 5, 13641−13655

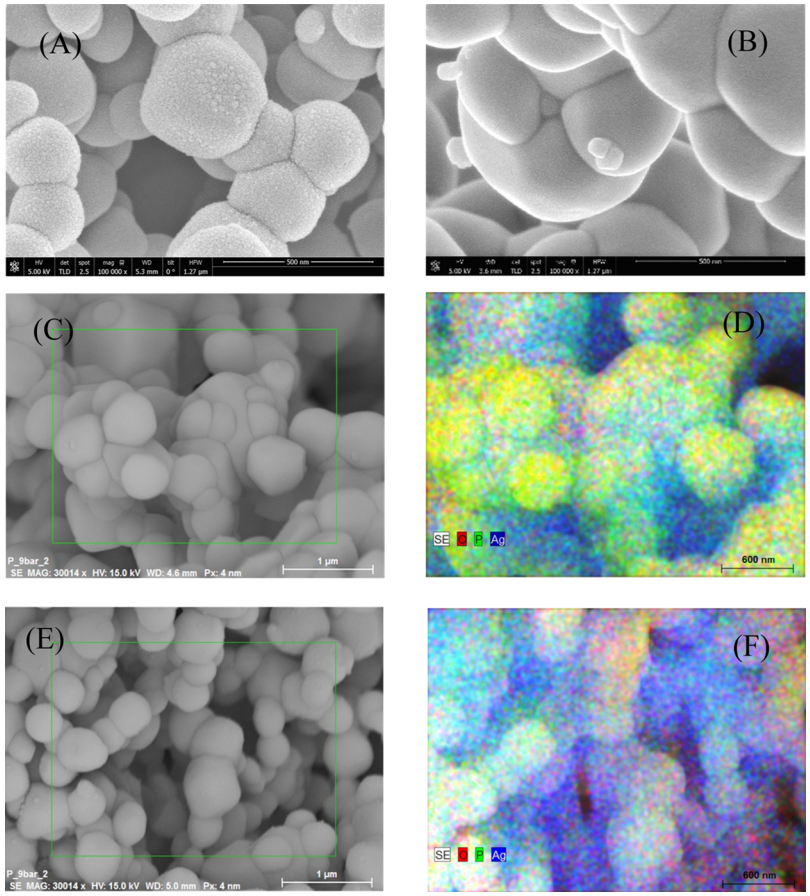

Figure 8. SEM images of (A) Ag_3PO_4 and (B) Ag−Ag_3PO_4. EDX mapping of (C,D) Ag_3PO_4 and (E,F) Ag−Ag_3PO_4 (F, MW = 3 min).

11 and 12, the photocatalytic activity (k = 0.3914 min^{-1}) obtained from this sample was higher than that of Ag_3PO_4 but lower than that of [Ag−Ag_3PO_4(F,Heating)], [Ag−Ag_3PO_4(F,MW)], and [Ag−Ag_3PO_4(F)]. The concentration of Ag on the surface of [Ag−Ag_3PO_4(F-Decanting,MW)] was estimated through EDX (Figure 14A,C) as 55.2 wt %. This further proves that for optimum photocatalytic activity, both formaldehyde addition as the reducing agent and MW radiation as heating are needed together.

In the absence of formaldehyde, the precipitated Ag_3PO_4 was microwaved, and the photocatalytic activity was examined. Again, the photocatalytic activity of the microwaved Ag_3PO_4 [Ag_3PO_4(MW)] with a rate constant of 0.3474 min^{-1} was higher than that of Ag_3PO_4. This implies that microwaving also affected the photocatalytic activity. The SEM−EDX spectra of Ag_3PO_4(MW) are shown in Figure 14B,D. The concentration of Ag on the surface was estimated to be ca. 63.08 wt %.

From the results presented above, it can be concluded that modification of Ag_3PO_4 using formaldehyde and MW radiation resulted in an increase in Ag concentration on the surface of Ag_3PO_4, which enhanced the photocatalytic activity. The authors investigated the effect of Ag−Ag_3PO_4(F,MW)/dye weight ratio and catalyst concentration on the photocatalytic activity. The results are presented in Figure 15. Figure 15 is generated taking into consideration the time required to attain almost 100% dye removal by Ag−Ag_3PO_4(F,MW).

Generally, as the wt ratio of the photocatalyst/dye and photocatalyst concentration increased, the time required to attain complete removal of the dye decreased. With a minimum photocatalyst concentration of 0.125 g/L, the entire concentration of dye was removed within 20 min. Increasing the photocatalyst concentration decreased significantly the time required to attain 100% dye removal. The time for complete removal of dye leveled off (at 4 min) when the catalyst concentration was increased beyond 0.375 g/L. A similar trend was observed for the variation of wt ratio of photocatalyst/dye with time required for complete dye removal. The time required for complete dye removal leveled off at 4 min when the wt ratio of the photocatalyst/dye was increased beyond 75. These results are impressive because it implies that a smaller quantity of Ag−Ag_3PO_4(F,MW) is required to achieve complete dye removal. The excellent photocatalytic degradation efficiency of Ag−Ag_3PO_4(F,MW) could be attributed to the VB position and inductive effect of PO_4^{3-}. These promote efficient separation of photogenerated electrons and holes as well as the localized surface plasmon resonance of Ag nanoparticles.[25] The photostability of the composite photocatalyst was examined. The cycling degradation of rhodamine B dye by Ag−Ag_3PO_4(F,MW) is presented in Figure 16. It can be deduced from Figure 16 that the composite photocatalyst remained stable even after five cycles of repeated photoreaction. There was approximately 10% reduction in the photodegradation efficiency after five cycles.

The potential application of the synthesized Ag−Ag_3PO_4(F,MW) in degrading crude oil was examined. Crude oil was fractionated into benzene, *n*-hexane, and 1:1 v/v methanol/benzene-soluble fractions. Each of these components including the crude oil was subjected to photocatalysis using Ag−Ag_3PO_4(F,MW). In a typical experiment, 100 mg of the photocatalyst was added to crude oil or crude oil fraction

https://dx.doi.org/10.1021/acsomega.0c00670
ACS Omega 2020, 5, 13641−13655

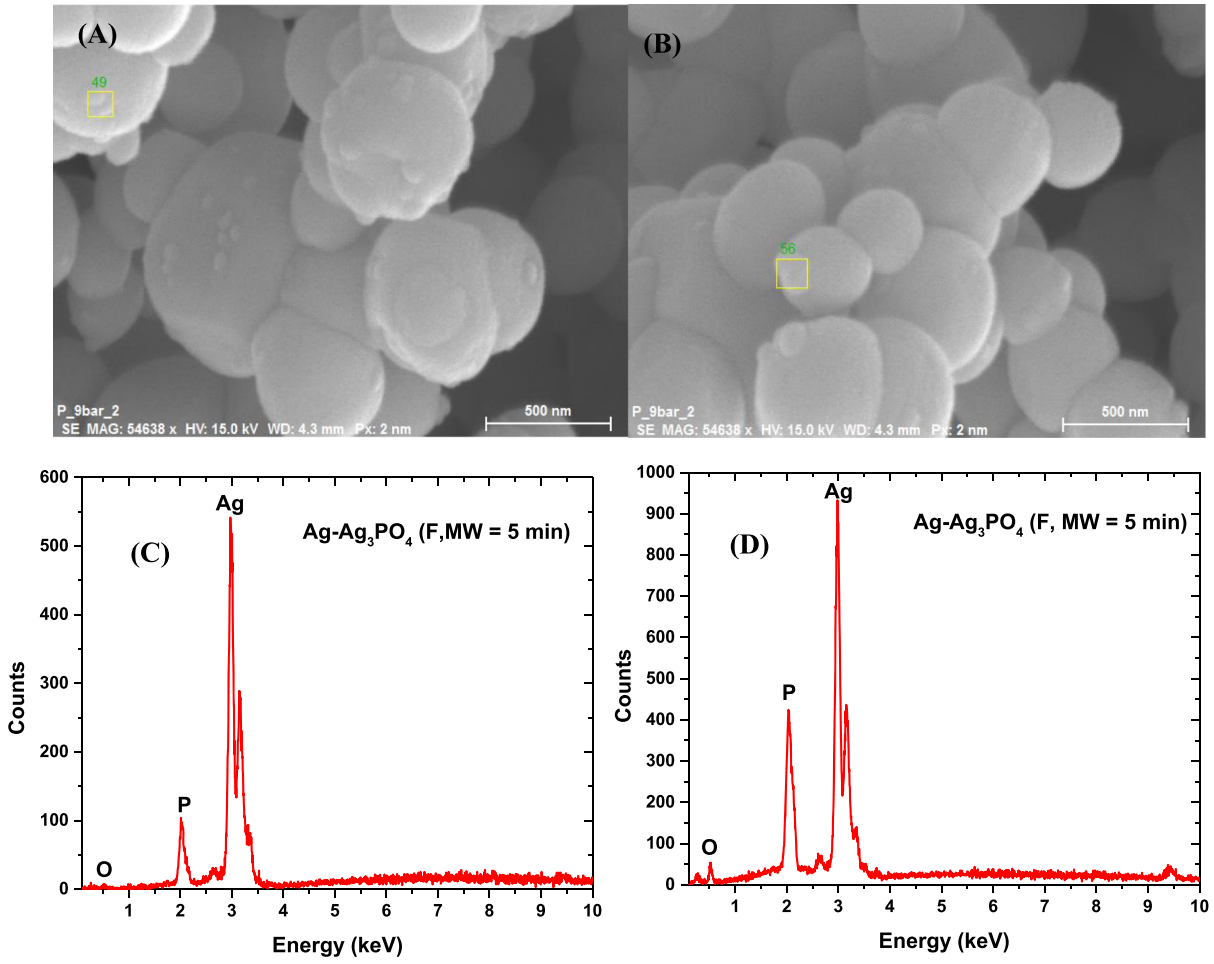

Figure 9. (A,B) SEM–EDX for Ag–Ag_3PO_4 (F, MW = 5 min), (C) EDX spectra for (A), and (D) EDX spectra for (B).

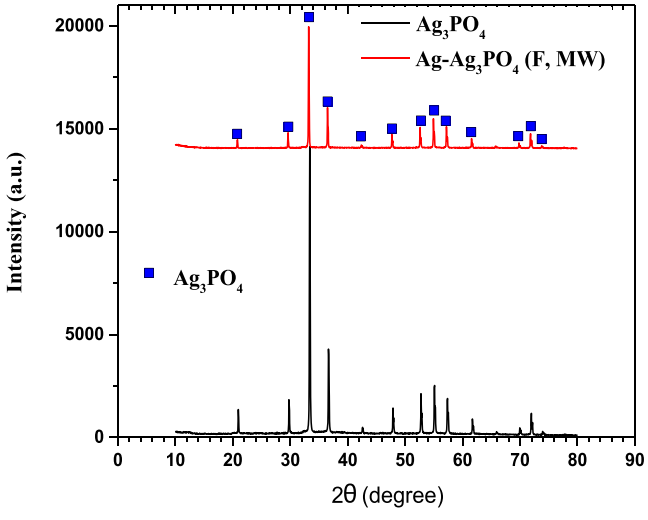

Figure 10. XRD pattern for Ag_3PO_4 and Ag_3PO_4(F,MW).

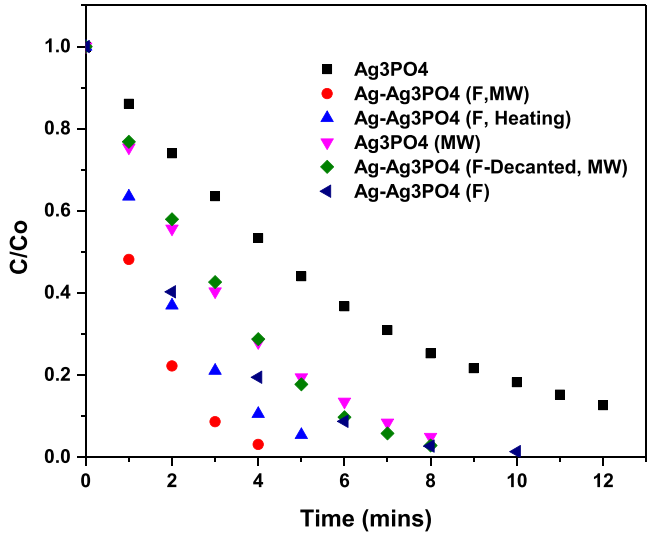

Figure 11. Photocatalytic activity of different Ag_3PO_4 and Ag–Ag_3PO_4-based photocatalysts synthesized under different experimental conditions.

(0.2 mL) and synthetic seawater (120 mL) and irradiated using solar energy (sunlight) for 6 h. The degraded crude oil or crude oil fraction was extracted with dichloromethane (DCM) and analyzed with UV–vis and GC/MS. The UV–vis spectra for the degraded and undegraded crude oil and crude oil fractions are presented in Figure 17. It can be inferred from Figure 17 that the concentration of the crude oil and the various crude oil fractions decreased significantly after exposure to sunlight and Ag–Ag_3PO_4(F,MW) for 6 h.

Ag–Ag_3PO_4(F,MW) was therefore effective at degrading crude oil. GC/MS analysis was conducted on the various crude oil fractions to identify the compounds that remained and

https://dx.doi.org/10.1021/acsomega.0c00670
ACS Omega 2020, 5, 13641–13655

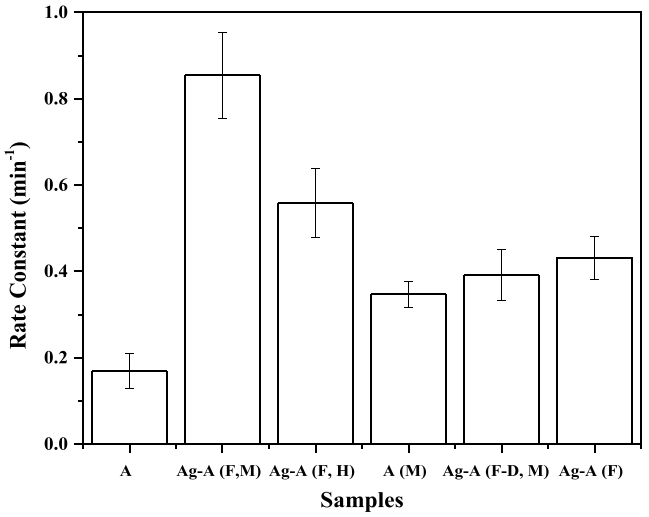

Figure 12. Rate constants for different Ag_3PO_4 and $Ag–Ag_3PO_4$-based photocatalysts synthesized under different experimental conditions. In the above plot: A = Ag_3PO_4, M = microwave (MW), H = heating, F = formaldehyde.

disappeared and intermediate compounds formed after photocatalysis. The chromatogram of the undegraded and degraded benzene-soluble fraction of the crude oil is presented in Figure 18. GC/MS analysis revealed the disappearance and the formation of new compounds. Nonadecane was the only compound found in both the degraded and undegraded benzene-soluble fractions. The undegraded benzene-soluble fractions contain several aromatics and paraffins. However, after the photocatalytic degradation, the aromatics: naphthalene-1-methyl (RT = 6.400 s), decahydro-4,4,8,9,10 penta methyl naphthalene (RT = 7.130 s), and naphthalene 1,4 dimethyl (RT = 7.745 s) disappeared, while a new aromatic compound diisooctyl phthalate (RT = 20.721 s) was formed. One noticeable observation was that though all the paraffins apart from nonadecane present in the benzene-soluble fraction disappeared after the photocatalysis, several new paraffinic compounds were formed. This implies that aromatics and cyclic alkanes are very sensitive to photocatalytic degradation and may be completely removed through photocatalysis, while the paraffins are less susceptible. Similar observation has been reported by D'Auria et al.[26] Because aromatic compounds present in the crude oil are sensitive to photocatalytic degradation while paraffins are easily remediated through biodegradation,[1h] a more efficient oil spill remediation strategy can be developed by combining photocatalysis and chemical dispersant application.

The GC/MS chromatogram of the undegraded crude oil fraction soluble in a 1:1 v/v methanol/benzene mixture is presented in Figure 19A. The undegraded fraction was made up of two paraffins: octadecane 2-methyl (RT = 17.974 s) and

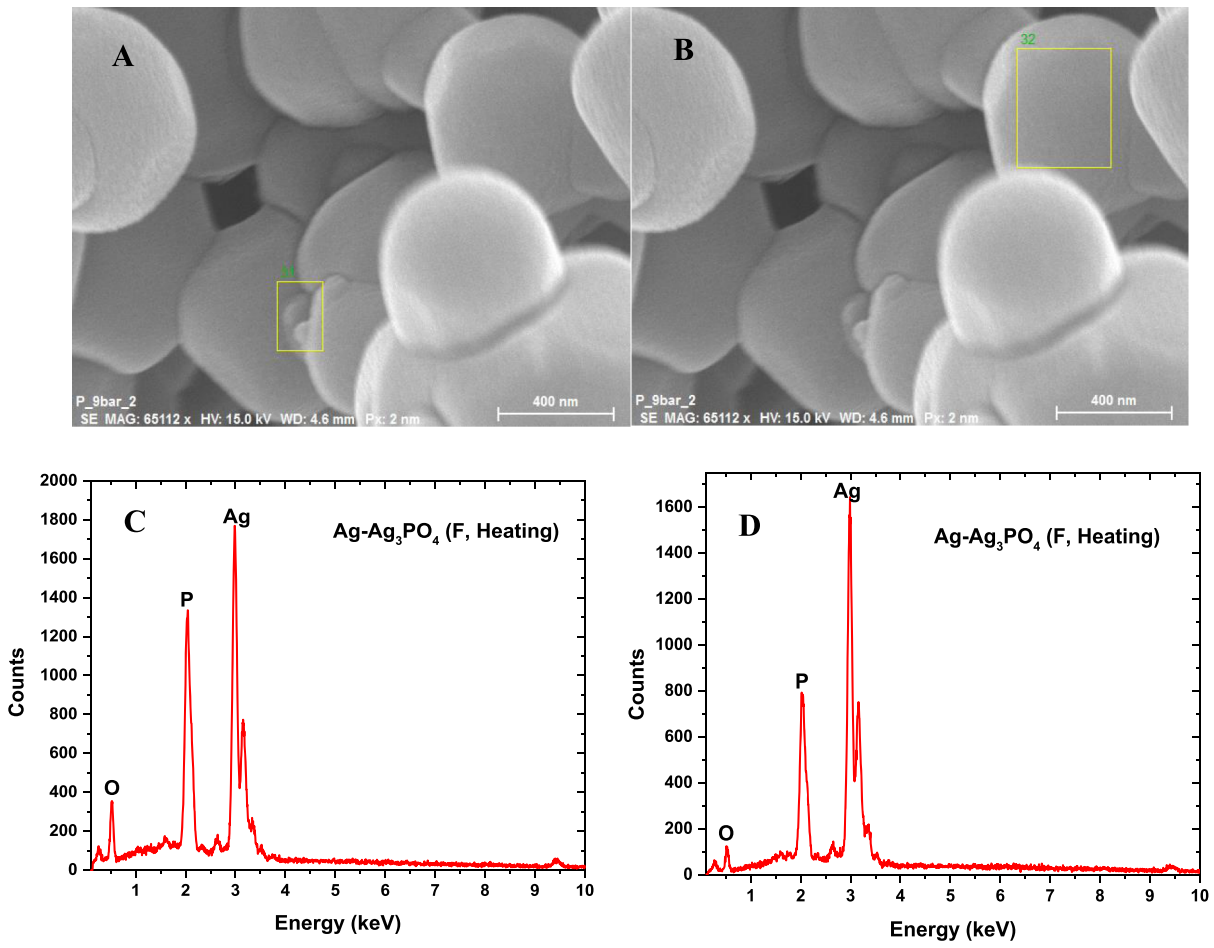

Figure 13. SEM–EDX for $Ag–Ag_3PO_4$(F,Heating). (A) Patches on Ag_3PO_4 (yellow rectangle) and (B) smooth surface of Ag_3PO_4 (yellow rectangle). EDX spectra for (C) (A) (patches) and (D) (B) (smooth surface).

https://dx.doi.org/10.1021/acsomega.0c00670
ACS Omega 2020, 5, 13641–13655

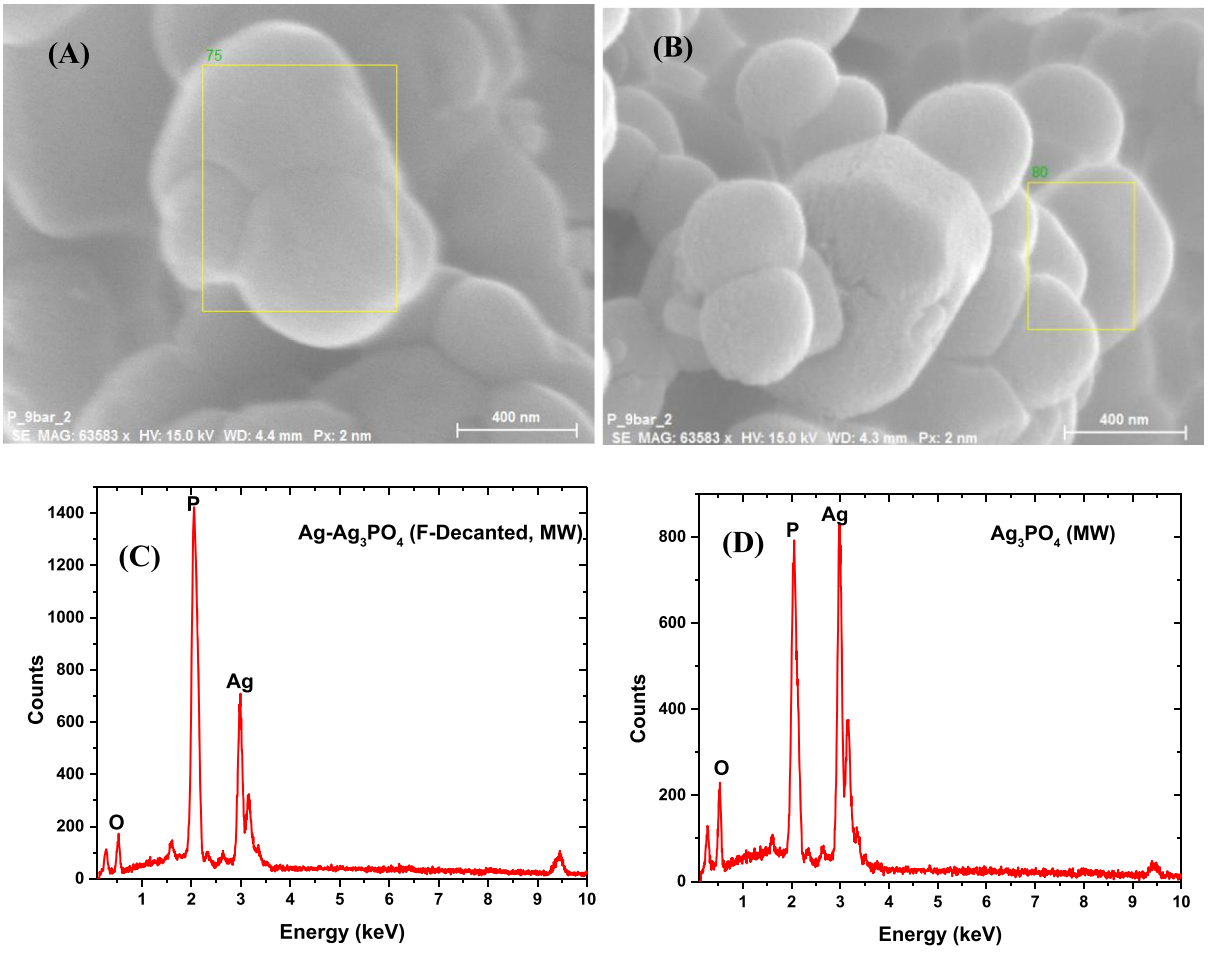

Figure 14. SEM−EDX image and spectra for (A,C) Ag−Ag_3PO_4(F-Decanted,MW) and (B,D) Ag_3PO_4(MW).

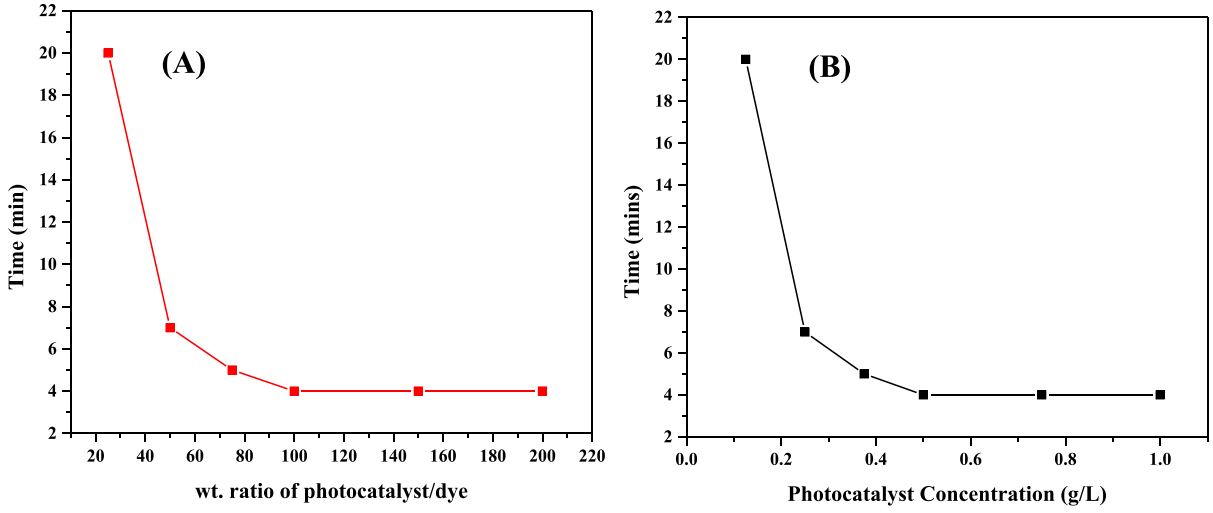

Figure 15. Effect of (A) wt ratio of the photocatalyst/dye and (B) photocatalyst concentration (g/L) on time required for Ag−Ag_3PO_4(F,MW) to attain ca. 100% dye removal.

octadecane 3-ethyl-5-(2-ehtylbutyl) (RT = 23.287 s) and several unidentified complex mixtures (UCMs). After photodegradation using Ag−Ag_3PO_4(F,MW), almost all the UCMs observed in Figure 19A were resolved, and several new compounds were formed (Figure 19B). The two paraffins identified in the undegraded fraction disappeared after the photocatalysis. However, several paraffins were identified in the degraded photoproducts formed.

The GC/MS chromatogram for the degraded and undegraded *n*-hexane-soluble fraction is presented in Figure 20. Most of the compounds identified in this fraction are paraffins. Three of the compounds were aromatics: benzocycloheptatriene (RT = 6.190 s), decahydro-4,4,8,9,10 pentam-

https://dx.doi.org/10.1021/acsomega.0c00670
ACS Omega 2020, 5, 13641−13655

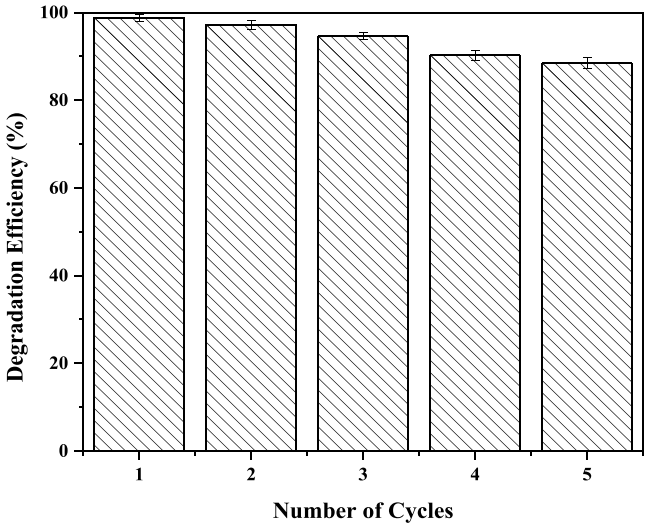

Figure 16. Recycled photodegradation experiment for Ag–Ag_3PO_4(F,MW).

ethylnaphthalene (RT = 7.345 s), and naphthalene 1,8 dimethyl (RT = 7.80). After degradation (Figure 20B), all the paraffins in the undegraded fraction disappeared except for nonadecane. The area under the nonadecane peak for the degraded and undegraded fractions was almost similar. Several new paraffins were identified in the degraded fraction. In addition, the three identified aromatics in the undegraded fraction also disappeared after photocatalysis. However, diisoodyl phthalate (RT = 20.776), a new aromatic compound, was formed after photocatalysis.

From the GC/MS results, it can be concluded that photocatalysis is effective at degrading completely aromatic components in crude oil while forming fewer aromatic compounds as photoproducts. On the other hand, though photocatalysis can degrade paraffins, it leads to the formation of several new paraffin compounds.

From the results presented above, Ag–Ag_3PO_4(F,MW) has excellent photocatalytic activity for the degradation of dyes and crude oil fractions. High degradation efficiency can be attained within shorter visible light exposure time even at relatively lower wt ratio of photocatalyst/dye and lower photocatalyst concentration. To understand the degradation mechanism, the radical and hole trapping experiment was conducted. The reactive specie(s) responsible for the efficient photocatalytic activity of Ag–Ag_3PO_4(F,MW) was examined using *t*-BuOH, benzoquinone, and EDTA–Na_2 as scavengers. Benzoquinone, *t*-BuOH, and EDTA–Na_2 serve as scavengers for superoxide radicals ($O_2^{\bullet-}$), hydroxyl radicals ($OH^{\bullet}$), and photogenerated holes (h^+), respectively. Addition of benzoquinone, *t*-BuOH,

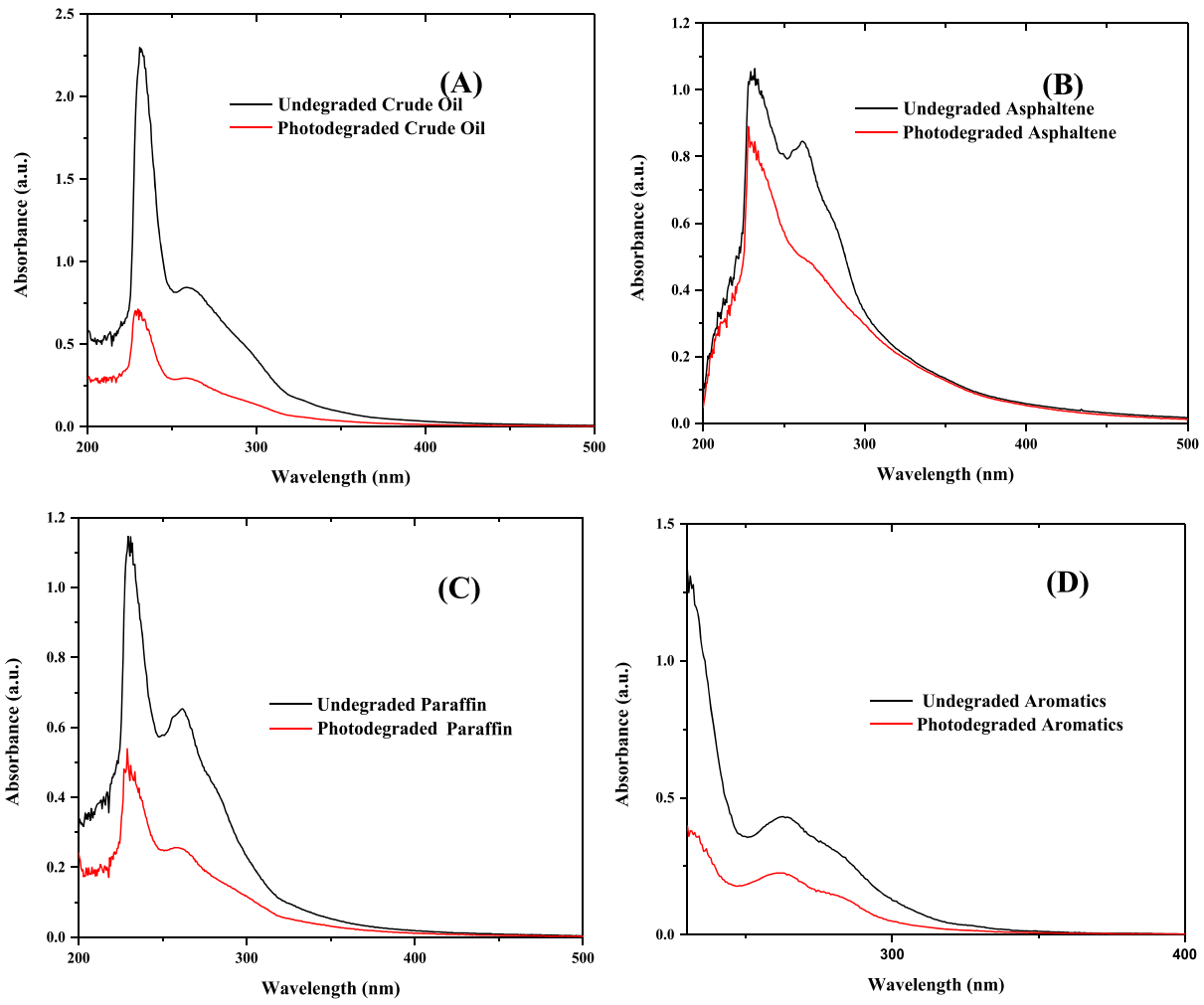

Figure 17. UV–vis absorption spectra for photodegraded and undegraded (A) crude oil, (B) asphaltene, (C) paraffin, and (D) aromatics.

https://dx.doi.org/10.1021/acsomega.0c00670
ACS Omega 2020, 5, 13641–13655

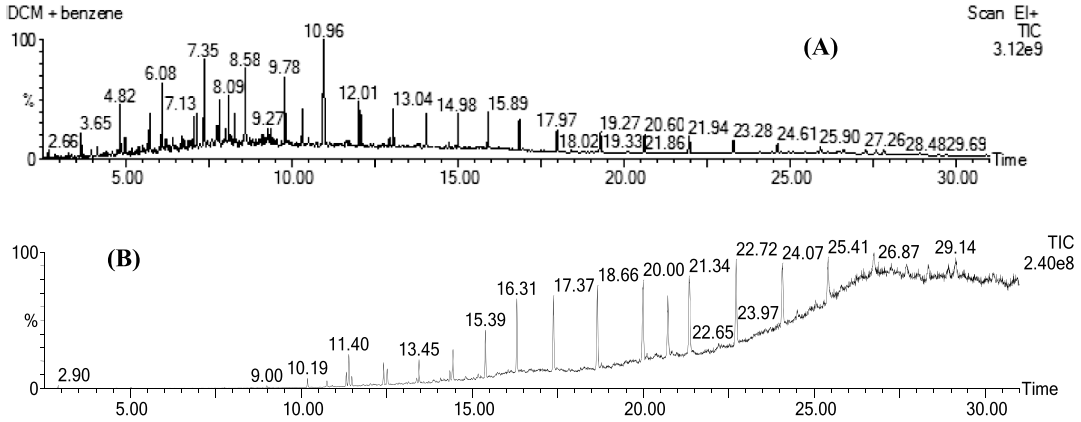

Figure 18. Chromatogram of benzene-soluble fraction (A) before and (B) after photocatalytic degradation with Ag−Ag_3PO_4(F,MW).

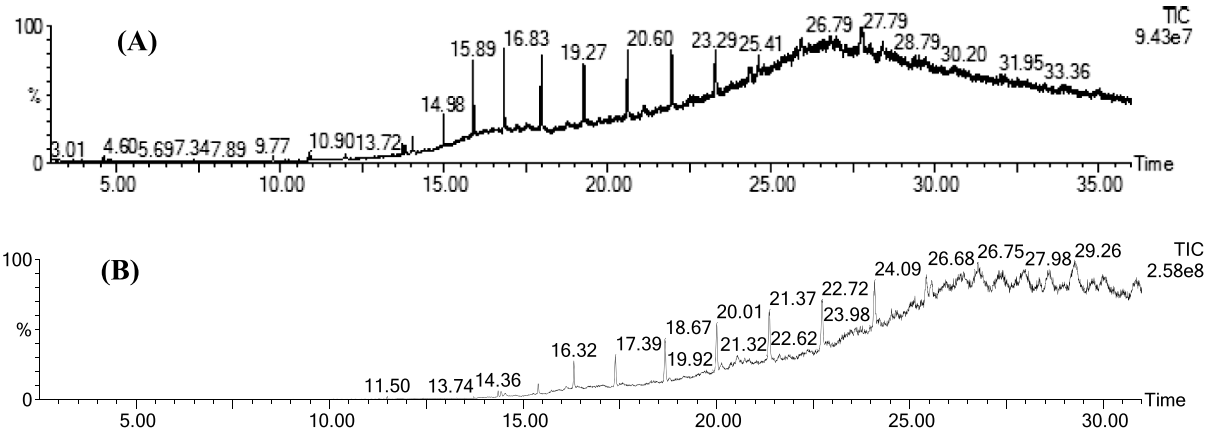

Figure 19. Chromatogram of 1:1 v/v methanol/benzene-soluble fraction of crude oil (A) before and (B) after photocatalytic degradation with Ag−Ag_3PO_4(F,MW).

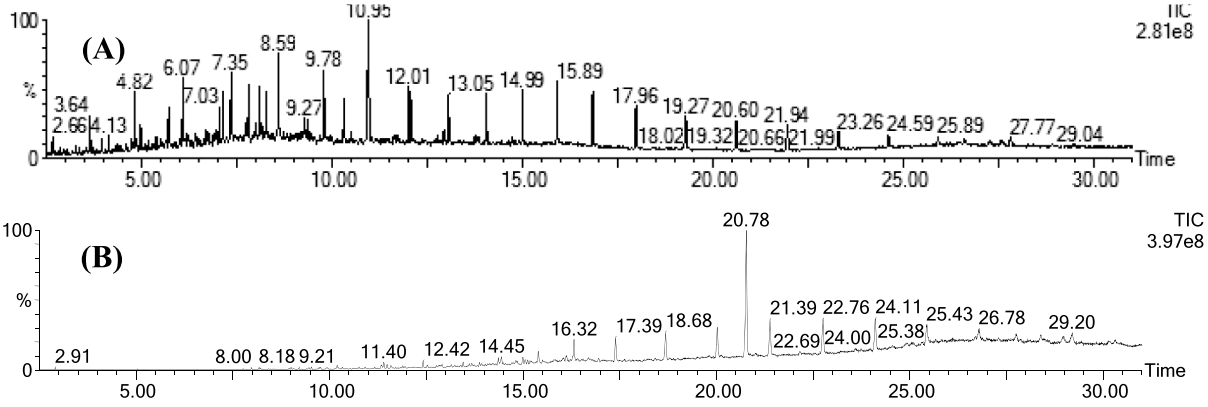

Figure 20. Chromatogram of *n*-hexane-soluble fraction (A) before and (B) after photocatalytic degradation with Ag−Ag_3PO_4(F,MW).

and EDTA−Na_2 reduced the photocatalytic efficiency from 98.1 to 48.2, 71.3, and 19.7%, respectively. This indicates that photogenerated holes (h^+) are the main reactive species responsible for the photodegradation of rhodamine B by Ag−Ag_3PO_4(F,MW). This observation is consistent with literature reports.[27] A possible photocatalytic degradation mechanism is presented below.

From the SEM−EDX images and analysis, a schematic diagram of the synthesized Ag−Ag_3PO_4 is presented in Figure 21A. Upon visible light irradiation, photons can be absorbed by both Ag_3PO_4 and Ag. This will result in the generation of electrons (e^-) and holes (h^+). The electrons in the VB of Ag_3PO_4 are then excited to the CB (Figure 20B). The localized surface plasmon effect produced by the collective oscillation of surface electrons on the Ag nanoparticles could generate a local inner magnetic field, which can enhance the separation of electrons and holes (Figure 21C,D). Because of the localized magnetic field and the good electron conductivity of Ag, the photogenerated electrons are quickly transferred from Ag_3PO_4.[7] Because the electrons are transferred far from the Ag^+ ions in Ag_3PO_4, the stability of Ag−Ag_3PO_4 is enhanced. That is, the electrons generated are transferred to the Ag

https://dx.doi.org/10.1021/acsomega.0c00670
ACS Omega 2020, 5, 13641−13655

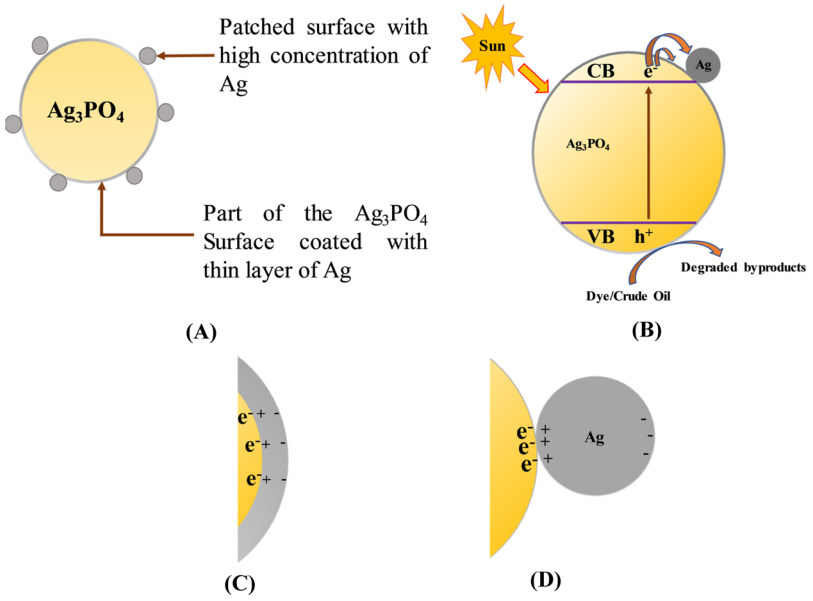

Figure 21. (A) Schematic of the Ag−Ag_3PO_4(F,MW) photocatalyst; schematic model for the (B) photocatalytic degradation of dyes/crude oil by Ag−Ag_3PO_4(F,MW), (C) electron entrapment by the Ag layer on Ag_3PO_4, and (D) electron entrapment by patches with high concentration of Ag.

nanoparticles with Ag acting as the electron acceptor. The photogenerated holes on the other hand remain on the surface of Ag_3PO_4 reducing the electron−hole recombination rate. Another possible explanation for the enhanced photocatalytic activity is presented as follows. Because Ag_3PO_4 is an n-type semiconductor, its Fermi level is close to the CB edge (4.95 eV). When the Ag−Ag_3PO_4 heterojunction is created, electrons flow from Ag_3PO_4 to Ag. The Ag−Ag_3PO_4 heterojunction results in an equilibration of the Fermi level. The new Fermi level attained from this equilibration is close to the CB of Ag_3PO_4.[28] Hence upon visible light irradiation, Ag acts as an electron acceptor, allowing the available photoexcited holes to be available for photocatalysis because the electron−hole recombination is reduced. Tastuma and Takada have reported that increase in electron concentration on the Ag nanoparticles resulting from the equilibration of the Fermi level may initiate a series of reduction reactions, while the high concentration of photoexcited holes on Ag_3PO_4 will initiate a series of photooxidation reactions that may result in the degradation of organic pollutants such as dyes and crude oil fractions.[29] Furthermore, the phosphate ions in Ag_3PO_4 have strong affinity for water. Hence, H_2O easily binds to the surface of Ag_3PO_4. With the presence of holes on Ag_3PO_4, hydroxyl radicals can be easily formed by the oxidation of H_2O molecules by holes.[30] These hydroxyl radicals oxidize dyes and crude oil fractions into photogenerated byproducts and ultimately carbon dioxide and water. However, the radical and hole trapping experiment revealed that photoexcited holes are the main reactive species responsible for the degradation of dyes; hence, the contribution from hydroxyl radicals may not be significant. The relatively lower photocatalytic activity of bare Ag_3PO_4 can be attributed to fast electron−hole recombination and the relatively lower photostability.

3. CONCLUSIONS

In summary, a highly efficient Ag−Ag_3PO_4 visible light photocatalyst was synthesized by an ion-exchange method and modified by using excess $AgNO_3$, formaldehyde, and MW radiation. The formaldehyde and MW radiation helped in the deposition of Ag on the surface of Ag_3PO_4 and the formation of high Ag-concentrated patches on the surface of Ag_3PO_4. Instead of MW radiation, a conventional heating method can be used but with a relatively reduced photocatalytic activity when compared with the composite photocatalyst synthesized with MW radiation. Ag−Ag_3PO_4 was stable and efficient for the degradation of rhodamine B dyes and crude oil fractions. GC/MS analysis of the photoproducts generated from the degradation of the crude oil fraction revealed that photocatalysis is effective in completely degrading aromatic components of crude oil with little generation of aromatic photoproducts. On the other hand, photodegradation of paraffins results in the generation of several paraffin photoproducts. The enhanced photocatalytic activity was attributed to the localized surface plasmon effect of Ag and the reduction of the electron−hole recombination.

4. EXPERIMENTAL SECTION

4.1. Materials. $AgNO_3$ (ACS reagent, ≥99%), Na_2HPO_4 (99.95%), rhodamine B dye (97%), benzene (analytical standard), hexane (laboratory reagent, ≥95%), methanol (HPLC 99.9%), and formaldehyde (37 wt % in H_2O) were purchased from Sigma-Aldrich, UK. Crude oil was obtained from Tullow Oil, Ghana.

4.2. Experimental Procedure. *4.2.1. Synthesis of Ag−Ag_3PO_4.* In a typical synthesis procedure for making the photocatalytic system, 50 mL of 0.05 M Na_2HPO_4 was added dropwise to 50 mL of 0.2 M $AgNO_3$ while stirring vigorously at ambient temperature. The resulting solution was stirred for 30 min while forming the Ag_3PO_4 precipitate. A known volume of formaldehyde solution was added and continuously stirred for another 30 min. The resulting solution with the precipitate was then subjected to MW radiation of 700 W at 2450 MHz for 3 min. The resulting (shown to be Ag−Ag_3PO_4) particles were collected by centrifugation and dried at 70 °C for 5 h. In another synthesis variant, after adding formaldehyde and stirring for 30 min, the resulting solution was heated in a water bath set at 80 °C for 3 min. The precipitate was collected by centrifugation and dried at 70 °C for 5 h. The effect of

https://dx.doi.org/10.1021/acsomega.0c00670
ACS Omega 2020, 5, 13641−13655

Table 1. Summary of Experimental Conditions Used for the Preparation of the Photocatalysts

sample	formaldehyde (F)	microwaving for 3 min (MW)	heating at 80 °C for 3 min (Heating)
Ag_3PO_4			
Ag_3PO_4(MW)		√	
Ag−Ag_3PO_4(F,W)	√	√	
Ag−Ag_3PO_4(F)	√		
Ag−Ag_3PO_4(F,Heating)	√		√
Ag−Ag_3PO_4(F-Decanted,MW)	√ (the resulting solution after the addition of F was decanted, and then the precipitates were dispersed in DI water and MW)	√	

formaldehyde (F) and MW or thermal heating on the resulting materials was investigated. The conditions for the experiments are summarized in Table 1.

4.2.2. Fractionating of Crude Oil. The crude oil was separated into three fractions. This was achieved by adding 50 mL of crude oil to 181 g of silica gel in a chromatographic column. *n*-Hexane (500 mL) was first added to the crude oil in the column to elute the *n*-hexane soluble fraction. Second, 500 mL of benzene was also added to the residual crude in the column for the elution of the benzene-soluble fraction. Last, a solution of 250 mL of methanol and 250 mL of benzene was again added to the residual crude after the second elution to elute the 1:1 v/v methanol/benzene-soluble fraction. The eluate samples of the various soluble fraction concentrates were formed by evaporating the solvent−crude oil fraction mixture using the rotary evaporator at 40 °C.

4.3. Product Characterization. *4.3.1. XRD.* The powder XRD patterns were obtained with a Bruker D8 ADVANCED focus diffractometer fitted with a position-sensitive detector (LynxEye) and a standard detector. Cu Kα radiation (λ = 0.15405 nm) and a 2θ angular range of 10−80° were used.

4.3.2. X-ray Photoelectron Spectroscopy. XPS of the Ag−Ag_3PO_4 sample was analyzed using a Kratos XSAM 800 photoelectron spectrometer connected with dual-anode X-ray source. Nonmonochromatic Mg Kα (1253.6 eV) X-ray source was used. The pressure in the analyzing chamber was less than 10^{-9} mbar. The sample spectra were analyzed using the CasaXPS software, and the peak shift due to any apparent charging was calibrated with respect to the C 1s peak set to 284.8 eV. A standard Shirley background with the product Gaussian (50%) and Lorentzian (50%) functions was used to fit each component spectrum.

4.3.3. Scanning Electron Microscopy with Energy-Dispersive X-ray Spectroscopy. The morphology of the synthesized nanocomposites was examined with a scanning electron microscope (FEI Nova NanoSem) connected to the EDX acquisition detector. The elemental composition was determined through EDX.

4.3.4. Diffuse Reflectance Spectroscopy (DRS). DRS was conducted using an Ocean Optics USB-4000 UV−vis spectrometer equipped with a dedicated reflectance probe. Glass slides were used to compress the synthesized nanocomposite into a flat film. The DRS measurement was conducted using polytetrafluoroethylene reflectance standard for reflectance calibration.

4.3.5. Photocatalytic Degradation of Rhodamine Blue. The photocatalytic activity of the synthesized Ag−Ag_3PO_4 was examined using rhodamine B dye. In a typical photocatalytic degradation test, 200 mL of rhodamine B solution (5 mg/L) in deionized water was used with an appropriate Ag−Ag_3PO_4 suspension concentration. A jacketed glass reactor with a quartz tube immersion well was used with illumination from a 300 W tungsten halogen lamp. For each of the experiments, the solution was stirred vigorously for 30 min in the dark to attain an adsorption−desorption equilibrium. An aliquot (2 mL) was removed at specific time intervals and centrifuged at 6000 rpm for 5 min to separate the powdered photocatalyst. The dye absorbance was measured using a UV−vis spectrophotometer (Ocean Optics 4000 USB) at an absorbance difference of 554−400 nm. The effect of photocatalyst concentration was examined by using varying amounts of Ag−Ag_3PO_4.

4.3.6. Photocatalytic Degradation of Crude Oil Fractions. The crude oil fraction (0.2 mL) was measured and added to 120 mL of synthetic seawater in a 200 mL beaker. The photocatalyst (100 mg) was added to the mixture of the crude oil fraction and distilled water. The resultant mixture was irradiated under sunlight with continuous stirring at 350 rpm to ensure that the photocatalyst is dispersed well in the water−crude oil mix. Irradiation was carried out continuously for 6 h, after which 10 mL of DCM was added to the resultant mixture to dissolve the degraded crude oil. DCM with the dissolved degraded crude oil fraction was separated from the photocatalyst and synthetic seawater using a separation funnel. The dissolved oil is further centrifuged at 6000 rpm for 15 min to ensure that all residual photocatalyst particles are separated. DCM with the dissolved crude oil fractions was characterized with a UV−vis spectrometer and a GC−MS spectrometer.

4.3.7. Gas Chromatography−Mass Spectrometry. DCM with the dissolved crude oil fraction was analyzed with GC/MS to identify the degraded byproducts from the photocatalysis. The following GC/MS conditions were employed; the oven was heated to an initial temperature of 80 °C, then ramped at 10 °C/min to 240 °C, held for 2 min, then ramped at 5 °C/min to 280 °C, and held for10 min; the injection temperature selected was 250 °C, with an injected volume of 0 μL. The split ratio used was 20:1. Helium was selected as the carrier gas. The solvent delay time was 2.50 min. The transfer temperature used was 250 °C, while the source temperature was 150 °C. The GC/MS column dimension was 27.0 m × 250 μm.

AUTHOR INFORMATION

Corresponding Author

Emmanuel Nyankson − *Department of Materials Science and Engineering, University of Ghana, LG 77 Accra, Ghana; Department of Materials Science and Metallurgy, University of Cambridge, CB3 0FS Cambridge, U.K.;* orcid.org/0000-0001-7041-3466; Email: enyankson@ug.edu.gh

Authors

Reuben Amedalor − *Department of Materials Science and Engineering, University of Ghana, LG 77 Accra, Ghana*

https://dx.doi.org/10.1021/acsomega.0c00670
ACS Omega 2020, 5, 13641−13655

Gauthaman Chandrabose − *School of Engineering and Innovation, The Open University, MK7 6AA Milton Keynes, U.K.*

Michael Coto − *Department of Materials Science and Metallurgy, University of Cambridge, CB3 0FS Cambridge, U.K.*

Satheesh Krishnamurthy − *School of Engineering and Innovation, The Open University, MK7 6AA Milton Keynes, U.K.;* orcid.org/0000-0001-7237-9206

R. Vasant Kumar − *Department of Materials Science and Metallurgy, University of Cambridge, CB3 0FS Cambridge, U.K.*

Complete contact information is available at: https://pubs.acs.org/10.1021/acsomega.0c00670

Notes

The authors declare no competing financial interest.

■ ACKNOWLEDGMENTS

The authors acknowledge the support from The Cambridge Africa Partnership for Research Excellence (CAPREx) program and Cambridge Africa Alborada Fund.

■ REFERENCES

(1) (a) Owoseni, O.; Nyankson, E.; Zhang, Y.; Adams, S. J.; He, J.; McPherson, G. L.; Bose, A.; Gupta, R. B.; John, V. T. Release of surfactant cargo from interfacially-active halloysite clay nanotubes for oil spill remediation. *Langmuir* **2014**, *30*, 13533−13541. (b) Nyankson, E.; Olasehinde, O.; John, V. T.; Gupta, R. B. Surfactant-loaded halloysite clay nanotube dispersants for crude oil spill remediation. *Ind. Eng. Chem. Res.* **2015**, *54*, 9328−9341. (c) Nyankson, E.; DeCuir, M. J.; Gupta, R. B. Soybean lecithin as a dispersant for crude oil spills. *ACS Sustainable Chem. Eng.* **2015**, *3*, 920−931. (d) Nyankson, E.; Demir, M.; Gonen, M.; Gupta, R. B. Interfacially active hydroxylated soybean lecithin dispersant for crude oil spill remediation. *ACS Sustainable Chem. Eng.* **2016**, *4*, 2056−2067. (e) Owoseni, O.; Nyankson, E.; Zhang, Y.; Adams, D. J.; He, J.; Spinu, L.; McPherson, G. L.; Bose, A.; Gupta, R. B.; John, V. T. Interfacial adsorption and surfactant release characteristics of magnetically functionalized halloysite nanotubes for responsive emulsions. *J. Colloid Interface Sci.* **2016**, *463*, 288−298. (f) Efavi, J. K.; Nyankson, E.; Yaya, A.; Agyei-Tuffour, B. Effect of Magnesium and Sodium Salts on the Interfacial Characteristics of Soybean Lecithin Dispersants. *Ind. Eng. Chem. Res.* **2017**, *56*, 12608−12620. (g) Nyankson, E.; Ober, C. A.; DeCuir, M. J.; Gupta, R. B. Comparison of the effectiveness of solid and solubilized dioctyl sodium sulfosuccinate (DOSS) on oil dispersion using the baffled flask test, for crude oil spill applications. *Ind. Eng. Chem. Res.* **2014**, *53*, 11862−11872. (h) Nyankson, E.; Rodene, D.; Gupta, R. B. Advancements in crude oil spill remediation research after the Deepwater Horizon oil spill. *Water, Air, Soil Pollut.* **2016**, *227*, 29. (i) Nyankson, E.; Agyei-Tuffour, B.; Efavi, J. K.; Yaya, A.; Onwona-Agyeman, B.; Sasu Konadu, D.; Amedalor, R.; Frimpong, B. K.; Bensah, Y. D. Potential Application of Dioctyl Sodium Sulfosuccinate Salt (DOSS)-Saponin Binary Dispersant in Oil Spill Remediation: Synergistic Interaction Between DOSS and Saponin. *Water, Air, Soil Pollut* **2020**, *231*, 76.

(2) Whitehead, A.; Dubansky, B.; Bodinier, C.; Garcia, T. I.; Miles, S.; Pilley, C.; Raghunathan, V.; Roach, J. L.; Walker, N.; Walter, R. B.; Rice, C. D.; Galvez, F. Genomic and physiological footprint of the Deepwater Horizon oil spill on resident marsh fishes. *Proc. Natl. Acad. Sci. U.S.A.* **2012**, *109*, 20298−20302.

(3) Nyankson, E.; Efavi, J. K.; Yaya, A.; Manu, G.; Asare, K.; Daafuor, J.; Abrokwah, R. Y. Synthesis and characterisation of zeolite-A and Zn-exchanged zeolite-A based on natural aluminosilicates and their potential applications. *Cogent Engineering* **2018**, *5*, 1440480.

(4) Dodoo-Arhin, D.; Buabeng, F. P.; Mwabora, J. M.; Amaniampong, P. N.; Agbe, H.; Nyankson, E.; Obada, D. O.; Asiedu, N. Y. The effect of titanium dioxide synthesis technique and its photocatalytic degradation of organic dye pollutants. *Heliyon* **2018**, *4*, No. e00681.

(5) (a) Anandan, S.; Vinu, A.; Mori, T.; Gokulakrishnan, N.; Srinivasu, P.; Murugesan, V.; Ariga, K. Photocatalytic degradation of 2,4,6-trichlorophenol using lanthanum doped ZnO in aqueous suspension. *Catal. Commun.* **2007**, *8*, 1377−1382. (b) Nyankson, E.; Agyei-Tuffour, B.; Annan, E.; Yaya, A.; Mensah, B.; Onwona-Agyeman, B.; Amedalor, R.; Kwaku-Frimpong, B.; Efavi, J. K. Ag2CO3-halloysite nanotubes composite with enhanced removal efficiency for water soluble dyes. *Heliyon* **2019**, *5*, No. e01969. (c) Nyankson, E.; Kumar, R. V. Removal of water-soluble dyes and pharmaceutical wastes by combining the photocatalytic properties of Ag3PO4 with the adsorption properties of halloysite nanotubes. *Mater. Today Adv.* **2019**, *4*, 100025. (d) Agbe, H.; Nyankson, E.; Raza, N.; Dodoo-Arhin, D.; Chauhan, A.; Osei, G.; Kumar, V.; Kim, K.-H. Recent advances in photoinduced catalysis for water splitting and environmental applications. *J. Ind. Eng. Chem.* **2019**, *72*, 31−49. (e) Nyankson, E.; et al. Synthesis and Application of Fe-Doped TiO2-Halloysite Nanotubes Composite and Their Potential Application in Water Treatment. *Adv. Mater. Sci. Eng.* **2019**, *2019*, 4270310. (f) Kusutaki, T.; Katsumata, H.; Tateishi, I.; Kaneco, M. Tetrahedral UMOFNs/Ag3PO4 Core-Shell Photocatalysts for Enhanced Photocatalytic Activity under Visible Light. *ACS Omega* **2019**, *4*, 15975−15984.

(6) Fujishima, A.; Honda, K. Electrochemical photolysis of water at a semiconductor electrode. *Nature* **1972**, *238*, 37.

(7) Liu, Y.; Fang, L.; Lu, H.; Li, Y.; Hu, C.; Yu, H. One-pot pyridine-assisted synthesis of visible-light-driven photocatalyst Ag/Ag3PO4. *Appl. Catal., B* **2012**, *115-116*, 245−252.

(8) (a) Martin, D. J.; Liu, G.; Moniz, S. J. A.; Bi, Y.; Beale, A. M.; Ye, J.; Tang, J. Efficient visible driven photocatalyst, silver phosphate: performance, understanding and perspective. *Chem. Soc. Rev.* **2015**, *44*, 7808−7828. (b) Murphy, A.; Barnes, P.; Randeniya, L.; Plumb, I.; Grey, I.; Horne, M.; Glasscock, J. Efficiency of solar water splitting using semiconductor electrodes. *Int. J. Hydrogen Energy* **2006**, *31*, 1999−2017.

(9) (a) Wang, J.; Liu, C.; Yang, S.; Lin, X.; Shi, W. Fabrication of a ternary heterostructure $BiVO_4$ quantum dots/C60/g-C_3N_4 photocatalyst with enhanced photocatalytic activity. *J. Phys. Chem. Solids* **2020**, *136*, 109164. (b) Lin, X.; Liu, C.; Wang, J.; Yang, S.; Shi, J. Graphitic carbon nitride quantum dots and nitrogen-doped carbon quantum dots co-decorated with BiVO4 microspheres: A ternary heterostructure photocatalyst for water purification. *Sep. Purif. Technol.* **2019**, *226*, 117−127.

(10) Yi, Z.; Ye, J.; Kikugawa, N.; Kako, T.; Ouyang, S.; Stuart-Williams, H.; Yang, H.; Cao, J.; Luo, W.; Li, Z. An orthophosphate semiconductor with photooxidation properties under visible-light irradiation. *Nat. Mater.* **2010**, *9*, 559.

(11) Bard, A. *Standard Potentials in Aqueous Solution*; Routledge, 2017.

(12) (a) Nayak, S.; Parida, K. M. Dynamics of Charge-Transfer Behavior in a Plasmon-Induced Quasi- Type-II p−n/n−n Dual Heterojunction in Ag@Ag3PO4/g-C3N4/NiFe LDH Nanocomposites for Photocatalytic Cr(VI) Reduction and Phenol Oxidation. *ACS Omega* **2018**, *3*, 7324−7343. (b) Shi, W.; Li, M.; Huang, X.; Ren, H.; Yan, C.; Guo, F. Facile synthesis of 2D/2D Co3(PO4) 2/g-C3N4 heterojunction for highly photocatalytic overall water splitting under visible light. *Chem. Eng. J.* **2020**, *382*, 122960.

(13) (a) Awazu, K.; Fujimaki, M.; Rockstuhl, C.; Tominaga, J.; Murakami, H.; Ohki, Y.; Yoshida, N.; Watanabe, T. A plasmonic photocatalyst consisting of silver nanoparticles embedded in titanium dioxide. *J. Am. Chem. Soc.* **2008**, *130*, 1676−1680. (b) Wang, P.; Huang, B.; Qin, X.; Zhang, X.; Dai, Y.; Wei, J.; Whangbo, M.-H. Ag@AgCl: A Highly Efficient and Stable Photocatalyst Active under Visible Light. *Angew. Chem., Int. Ed.* **2008**, *47*, 7931−7933.

(14) Tian, J.; Yan, T.; Qiao, Z.; Wang, L.; Li, W.; You, J. Anion-exchange synthesis of Ag2S/Ag3PO4 core/shell composites with enhanced visible and NIR light photocatalytic performance and the photocatalytic mechanisms. *Appl. Catal., B* **2017**, *209*, 566−578.
(15) (a) Shi, W.; Li, M.; Huang, X.; Ren, H.; Guo, F. Three-dimensional Z-Scheme Ag3PO4/Co3(PO4)2@Ag heterojunction for improved visible-light photocatalytic degradation activity of tetracycline. *J. Alloys Compd.* **2020**, *818*, 152883. (b) Tang, H.; Fu, Y.; Chang, S.; Xie, S. Construction of Ag 3 PO 4 /Ag 2 MoO 4 Z-scheme heterogeneous photocatalyst for the remediation of organic pollutants. *Chin. J. Catal.* **2017**, *38*, 337−347.
(16) Hou, Y.; Zuo, F.; Ma, Q.; Wang, C.; Bartels, L.; Feng, P. Ag3PO4 oxygen evolution photocatalyst employing synergistic action of Ag/AgBr nanoparticles and graphene sheets. *J. Phys. Chem. C* **2012**, *116*, 20132−20139.
(17) (a) Liu, Y.; Fang, L.; Lu, H.; Liu, L.; Wang, H.; Hu, C. Highly efficient and stable Ag/Ag3PO4 plasmonic photocatalyst in visible light. *Catal. Commun.* **2012**, *17*, 200−204. (b) Gondal, M. A.; Chang, X.; Sha, W. E. I.; Yamani, Z. H.; Zhou, Q. Enhanced photoactivity on Ag/Ag3PO4 composites by plasmonic effect. *J. Colloid Interface Sci.* **2013**, *392*, 325−330.
(18) Liu, Y.; Yang, D.; Xu, T.; Shi, Y.; Song, L.; Yu, Z.-Z. Continuous photocatalytic removal of chromium (VI) with structurally stable and porous Ag/Ag3PO4/reduced graphene oxide microspheres. *Chem. Eng. J.* **2020**, *370*, 122200.
(19) Coto, M.; Divitini, G.; Dey, A.; Krishnamurthy, S.; Ullah, N.; Ducati, C.; Kumar, R. V. Tuning the properties of a black TiO 2 -Ag visible light photocatalyst produced by a rapid one-pot chemical reduction. *Mater. Today Chem.* **2017**, *4*, 142−149.
(20) Teng, W.; Li, X.; Zhao, Q.; Chen, G. Fabrication of Ag/Ag3PO4/TiO2 heterostructure photoelectrodes for efficient decomposition of 2-chlorophenol under visible light irradiation. *J. Mater. Chem. A* **2013**, *1*, 9060−9068.
(21) Krause, M. O.; Ferreira, J. G. K X-ray emission spectra of Mg and Al. *J. Phys. B: At. Mol. Phys.* **1975**, *8*, 2007.
(22) Zhang, W.; Zhou, L.; Shi, J.; Deng, H. Synthesis of Ag3PO4/G-C3N4 Composite with Enhanced Photocatalytic Performance for the Photodegradation of Diclofenac under Visible Light Irradiation. *Catalysts* **2018**, *8*, 45.
(23) Bafaqeer, A.; Tahir, M. Well-designed ZnV2O6/g-C3N4 2D/2D nanosheets heterojunction with faster charges separation via pCN as mediator towards enhanced photocatalytic reduction of CO2 to fuels. *Appl. Catal., B* **2019**, *242*, 312−326.
(24) Stuerga, D.; Delmotte, M.; Strauss, C. R.; Perreux, L.; Loupy, A.; Gedye, R. N.; Petit, A.; Bogdal, D. *Microwaves in Organic Synthesis*; WILEY-VCH Verlag, 2006.
(25) Pan, C.; Zhu, Y. New type of BiPO4 oxy-acid salt photocatalyst with high photocatalytic activity on degradation of dye. *Environ. Sci. Technol.* **2010**, *44*, 5570−5574.
(26) D'Auria, M.; Emanuele, L.; Racioppi, R.; Velluzzi, V. Photochemical degradation of crude oil: Comparison between direct irradiation, photocatalysis, and photocatalysis on zeolite. *J. Hazard. Mater.* **2009**, *164*, 32−38.
(27) Yan, T.; Zhang, H.; Liu, Y.; Guan, W.; Li, J.; You, J.W. Fabrication of robust M/Ag3PO4(M = Pt, Pd, Au) Schottky-type heterostructures for improved visible-light photocatalysis. *RSC Adv.* **2014**, *4*, 37220−37230.
(28) Hu, H.; Jiao, Z.; Wang, T.; Ye, J.; Lu, G. Enhanced photocatalytic activity of Ag/Ag3PO4 coaxial hetero-nanowires. *J. Mater. Chem. A* **2013**, *1*, 10612−10616.
(29) Tatsuma, T.; Takada, K. UV-Light-Induced Swelling and Visible-Light-Induced Shrinking of a TiO2-Containing Redox Gel. *Adv. Mater.* **2007**, *19*, 1249−1251.
(30) Teng, W.; Li, X.; Zhao, Q.; Zhao, J.; Zhang, D. In situ capture of active species and oxidation mechanism of RhB and MB dyes over sunlight-driven Ag/Ag3PO4 plasmonic nanocatalyst. *Appl. Catal., B* **2012**, *125*, 538−545.

https://dx.doi.org/10.1021/acsomega.0c00670
ACS Omega 2020, 5, 13641−13655